

1 **Simultaneous OI 630 nm imaging observations of thermospheric gravity waves and**
2 **associated revival of fossil depletions around midnight near the EIA crest**

3
4
5 **Authors:**

6 **1. Navin Parihar**

7 Indian Institute of Geomagnetism, Navi Mumbai, India

8 e-mail: navindeparihar@gmail.com

9
10 **2. Saranya Padincharapad**

11 (a) Equatorial Geophysical Research Laboratory, Indian Institute of Geomagnetism,
12 Tirunelveli, India

13 (b) Manonmaniam Sundaranar University, Tirunelveli, India

14 e-mail: anuja8494@gmail.com

15
16 **3. Anand Kumar Singh**

17 National Centre for Polar and Ocean Research, Goa, India

18 e-mail: singhaaks@gmail.com

19
20 **4. Prasanna Mahavarkar**

21 Indian Institute of Geomagnetism, Navi Mumbai, India

22 e-mail: mahavarkarprasanna@gmail.com

23
24 **5. A. P. Dimri**

25 Indian Institute of Geomagnetism, Navi Mumbai, India

26 e-mail: apdimri@hotmail.com

27
28 **Corresponding Author:**

29 **Navin Parihar**, Indian Institute of Geomagnetism, Navi Mumbai, India

30 e-mail: navindeparihar@gmail.com

31
32 **Key Words:**

33 Airglow imaging; Midnight Irregularities/Depletions; Gravity wave seeding; Low-
34 latitude ionosphere.

36 **Abstract**

37 We report the F-region airglow imaging of fossil plasma depletions around midnight that
38 revived afresh under the persisting thermospheric gravity wave (GW) activity. An all-sky
39 imager recorded these events in OI 630 nm imaging over Ranchi (23.3° N, 85.3° E, mlat. ~19°
40 N), India, on 16 April 2012. Northward propagating and east-west aligned GWs (λ ~210 km,
41 v ~64 m/s, and τ ~0.91 h) were seen around midnight. Persisting for ~2 hours, this GW
42 activity revived two co-existing and eastward drifting fossil depletions, DP1 and DP2. GWs-
43 driven revival was prominently seen in depletion DP1, wherein its apex height grew from
44 ~600 km to >800 km, and the level of intensity depletion increased from ~17% to 50%.
45 Present study is novel in the sense that simultaneous observations of thermospheric GWs
46 activity and associated evolution of depletion in OI 630 nm airglow imaging, and that too
47 around local midnight, have not been reported earlier. Current understanding is that GW
48 phase fronts aligned parallel to the geomagnetic field lines and eastward propagating are
49 more effective in seeding Rayleigh-Taylor (RT) instability. Here, GW fronts were east-west
50 aligned (i.e. perpendicular to the geomagnetic field lines) and propagated northward, yet they
51 revived fossil depletions.

52

53

54 **1. Introduction**

55 Gravity waves (GWs) are well-known to influence the mesosphere-lower thermosphere-
56 ionosphere (MLTI) region. GWs significantly contribute to the momentum and energy budget
57 of the MLT region via the wave-dissipation processes (Fritts and Alexander, 2003; Holton,
58 1983). Apart from the dominant solar and geomagnetic inputs, GWs are the key element in
59 some of the electrodynamic processes in the ionosphere e.g. irregularities, atmosphere-
60 ionosphere (AI) coupling, traveling ionospheric disturbances, etc.. In the equatorial F-region,
61 GWs modulate the ionospheric plasma into wave-like ionization structures. Under favourable
62 conditions, these structures act as a seed to Generalized Rayleigh-Taylor (GRT) instability
63 that generates the irregularities (Fritts et al., 2009; Huba and Joyce, 2007, 2010; Huba and
64 Liu, 2020; Hysell et al., 1990; Kelley, 2009; Woodman, 2009). GWs are also important in the
65 AI coupling during deep convection activity, thunderstorms, lightning, cyclones, tornadoes,
66 transient luminous events (TLEs)/sprites initiation, tsunamis, etc. (Azeem and Barlage, 2018;
67 Maurya et al., 2022; Huba et al., 2015). GWs can also generate medium-scale traveling
68 ionospheric disturbances (MSTIDs) (Fukushima et al., 2012; Figueiredo et al., 2018; Heale et
69 al., 2022, and references cited therein). On the course of their propagation, GWs can also
70 induce periodic fluctuations in the ionospheric parameters e.g. the electron density or total
71 electron content (TEC), the F-region height, temperatures and winds, etc. (Ford et al., 2006,
72 2008; Klausner et al., 2009; Parihar et al., 2018; Vadas and Azeem, 2021) or airglow
73 emission (Huba et al., 2015; Makela et al., 2011).

74

75 The crucial role of GWs in seeding the post-sunset equatorial spread-F (ESF) or plasma
76 bubbles (EPBs) is fairly well understood (Abdu et al., 2009; Fritts et al., 2009; Huba and
77 Joyce, 2007, 2010; Hysell et al., 1990; Kelley, 2009; Singh et al., 1997; Tsunoda, 2010;
78 Tulasi Ram et al., 2014; Woodman, 2009). However, their role in the seeding of the
79 midnight/post-midnight irregularities remains poorly understood, especially when the
80 important criteria for the triggering of the GRT instability are absent (e.g., the favorable
81 alignment of the solar terminator with the geomagnetic field lines and the pre-reversal
82 enhancement, PRE, of the zonal electric field). Lately, Huba and Liu (2020) reported the
83 global simulations of the ESF using the SAMI3/WACCM-X coupled model. SAMI3 is the
84 abbreviation for ‘*Sami3 is Another Model of Ionosphere*’ (Huba et al., 2008), and WACCM-
85 X stands for the ‘*Whole Atmosphere Community Climate Model with thermosphere and*
86 *ionosphere extension*’ (Liu et al., 2010). For the first time, Huba and Liu’s (2020) simulations
87 demonstrated that GWs are the dominant seed mechanism and can spontaneously generate

88 the ESF, and that the EPBs develop self-consistently in the postsunset ionosphere. Studies by
89 Nishioka et al. (2012) show that the GRT instability can occur near midnight under the
90 influence of enhanced GW activity and then can lead to the growth of irregularities. MSTIDs
91 are an important generation mechanism of post-midnight irregularities wherein the electric
92 field perturbations associated with them acts as the seed (Miller et al., 2009; Taori et al.,
93 2015). Otsuka (2018) have presented an elaborative review of these mechanisms. All-sky
94 airglow imaging (ASAI) along with the radar, ionosonde, and GPS measurements have
95 significantly contributed to our understanding of the crucial role of GWs in seeding the EPBs
96 (Mendillo and Baumgardner, 1982; Mendillo et al., 1997; Taori et al., 2010; Yadav et al.,
97 2017). *Spread-F Experiment (SpreadFEx)* carried out in Brazil during September-November
98 2005 is one such example (Fritts et al., 2009). In the Indian subcontinent, Sreeja et al. (2009)
99 reported the GWs in OI 630 nm dayglow intensity variations that acted as a seed to the ESF
100 irregularities.

101

102 GWs that give rise to the EPBs have usually been reported in the MLT region airglow
103 imaging (e.g. Fritts et al., 2009; Paulino et al., 2011; Takahashi et al., 2009; Taori et al.,
104 2013). Reports featuring them in the F-region airglow imaging are rare and limited to that of
105 Makela et al. (2011), Paulino et al. (2016, 2018), Sau et al. (2018), and Smith et al. (2015).
106 Makela et al. (2011) and Smith et al. (2015) reported the thermospheric imaging observations
107 of GWs associated with tsunami and earthquake, respectively. Paulino et al. (2016, 2018) and
108 Sau et al. (2018) presented their observations in OI 630 nm imaging from Brazil and India,
109 respectively. However, these authors did not report any occurrence of depletions during the
110 undergoing GW activity. We report, for the first time, simultaneous observations GWs and
111 depletions in the F-region airglow imaging.

112

113 On the course of temporary campaign-based ASAI observations of OI 630 nm emission
114 under *Climate And Weather of Sun-Earth System (CAWSES) India Phase II Programme*
115 at Ranchi (23.3° N, 85.3° E, mlat. ~19° N), GW activity and “fossil depletions” were seen
116 together on 16 April 2012 with the former reviving the latter. Fossil depletions are the
117 remnants of airglow depletion or EPBs that have ceased growing upward or poleward;
118 however, they continue to persist and move with ambient plasma drift. Under *Maui Middle*
119 *Atmosphere and Lower Thermosphere (Maui-MALT)* initiative, Makela et al. (2004) reported
120 their extensive observations in OI 630 nm imaging from Haleakala Volcano (20.7° N, 203.7°
121 E; mlat. 21.3° N), Hawaii during the solar maximum of 2002-2003. Chapagain et al. (2011)

122 presented their limited observations from Christmas Island (2.1° N, 157.4° W, mlat. 2.8° N)
123 during September 1995. In India, Sekar et al. (2007) presented their case study from Gadanki
124 (13.5° N, 79.2° E, mlat. 6.3° N). However, these investigations did not discuss any
125 resurgence of fossil depletions associated with the GW activity. Novelty of this study is that
126 the “fossil depletions” revived into “active depletions” after the emission layer witnessed the
127 GW activity. Lately, Wrasse et al. (2021) presented an interesting event wherein a fossil EPB
128 merged with other ones after interacting with an electrified MSTID and turned into an active
129 bubble.

130

131

132 **2. Instrumentation and data**

133 Under the *CAWSES India Phase II Programme*, an ASAI was installed for limited
134 nightglow observations at Ranchi (23.3° N, 85.3° E, mlat. $\sim 19^{\circ}$ N), located near the crest of
135 equatorial ionization anomaly (EIA) in India during April 2012. Parihar et al. (2017) and
136 Parihar (2019) have described this ASAI system in detail. OI 630 nm emission was
137 monitored using a 2.2 nm half-power bandwidth optical filter having transmittance of $\sim 77\%$.
138 Our imager’s field-of-view roughly covered about $7\text{-}8^{\circ}$ latitude/longitude region at 250 km
139 over Ranchi. Airglow images were flat-fielded to reduce the inhomogeneous contribution at
140 lower elevations due to van Rhijn effect and non-uniform sensitivity of CCD detector at
141 different pixels. Next, following the technique described by Wrasse et al. (2021), we
142 detrended the individual images to enhance the contrast of airglow features using an hour
143 running average image. Using known astral positions and assuming OI 630 nm emission peak
144 at 250 km, the geographic coordinates of each pixel was determined following the technique
145 of Garcia et al. (1997). Using this information, all-sky images were unwarped. We follow the
146 technique discussed by Pimenta et al. (2003) to determine the drift velocity of depletions.
147 First, for a given latitude, two intensity profiles along east-west direction as a function of
148 distance was generated using two successive unwarped images. Next, the east-west
149 displacement of depletion was estimated using these two profiles from which drift speed was
150 determined (see Pimenta et al., 2003 for details of this technique). Similarly, the propagation
151 characteristics of GW fronts were estimated by tracking faint crest and trough along the
152 propagation direction in the consecutive images. As GW fronts were unclear in images, we
153 used contrast-enhanced images. We, also, generated NS keograms to visualize GW traces and
154 determine their speed. A keogram is a time-versus-latitude plot generated by extracting a NS
155 column from individual images and stacking them horizontally. Next, GWs speed was, also,

156 estimated from the slope of wave traces seen in these keograms (Makela et al., 2006). We
157 looked into the total electron content (TEC) measurements from an *International GNSS*
158 *Service* station Hyderabad (17.3° N, 78.6° E, mlat. ~12.0° N, located nearby and south of
159 Ranchi) to ascertain GW activity seen in the ASAI observations (Source: <https://t-ict4d.ictp.it/nequick2/gnss-tec-calibration>,
160 Ciruolo et al., 2007). Quiet geomagnetic
161 conditions prevailed on this night with $Kp < 2$, $Ap = 4$, and $-4 < Dst < 10$ nT.

162
163

164 3. Observations

165 Such GWs-driven revival of “fossil depletions” was recorded in airglow images during 1700-
166 2000 UT on 16 April 2012. Here, Indian Standard Time (IST) = Universal Time (UT) + 0530
167 and Local Time (LT) \approx IST. As such, 1700-2000 UT corresponds to ~1.5 h duration before
168 and after the local midnight. Figures 1 and 2 present airglow images that depict this event
169 seen over Ranchi during 1742-1942 UT on 16 April 2012. As the faint airglow features were
170 getting lost in the unwarping process, warped all-sky images are presented. Supplementary
171 material S1 shows the movie created from these images that feature this event. Fossil
172 depletions of our interest that showed the GWs-driven revival are marked as **DP1** and **DP2** in
173 Figure 1 and 2. Here, **ROI1** is the region-of-interest wherein a few weakly perceivable fronts
174 of GWs and fossil depletions coexisted initially.

175

176 3.1 Signatures of GW activity in the F-region

177 We first observed faint signatures of GW activity near the southern edge of the field-of-view
178 (FOV) during ~1715-1724 UT. Successive images showed unclear signatures of GWs
179 activity. Starting ~1730 UT, their presence became more evident and continued until 1906
180 UT or so. GWs fronts were not clearly seen because of their interaction with co-existing
181 depletions. Some weakly perceivable bright fronts are marked as ‘f1’, ‘f2’, ‘f3’ and ‘f4’ in
182 Figure 1 and 2. Similarly, dark trough that precede fronts ‘f1’ and ‘f2’ are marked as ‘t1’ and
183 ‘t2’, respectively. Often GWs in OI 630 nm imaging are faint and unclear. Under similar
184 situations, Makela et al. (2011) found that time difference (TD) images have proven ability to
185 reflect such GWs faint fronts. In their work, initial analysis of raw images did not show any
186 GWs activity linked with tsunami; however, TD images indeed reflected associated GWs. We
187 generated such TD images and are shown in Figure 3 which clearly show dark troughs ‘t1’
188 and ‘t2’ and GW fronts ‘f1’ and ‘f2’. North-south (NS) keograms [shown in Figure 4 (a) and

189 (b)] showed a few clear alternating bright and dark intensity striations over the north, and
190 their slope indicates that GWs propagated towards the north. We estimated GWs propagation
191 characteristics using the slope of wave traces (marked by black arrow 'b1', 'b2', 'b3', 'b4') in
192 keograms and cross-verified them with the intensity profiling technique. We found that these
193 GWs propagated from the south to north with the phase speed (v) of $\sim 64 \pm 2$ m/s and had the
194 horizontal wavelength (λ) and period (τ) of $\sim 210 \pm 6$ km and $\sim 0.91 \pm 0.06$ h, respectively.

195

196 We further looked into the TEC measurements from IGS station Hyderabad (17.3° N, 78.6°
197 E, mlat. $\sim 12.0^\circ$ N), India to confirm this on-going GWs activity. Figure 5 shows the TEC
198 measurements depicting GW activity in and around Hyderabad during 1700-2000 UT on this
199 night. Figure 5 (a) shows the scatter plots of the TEC along the trajectory of ionospheric
200 pierce points (IPPs) for different GPS satellites during 1700-1930 UT on this night. PRN
201 numbers of GPS satellites, along with the start time at 1700 UT, are indicated next to the
202 corresponding IPPs trajectory. TEC variations along the NS-aligned IPPs tracks (e.g. G27
203 and G28) clearly show the wavelike fluctuations in the 15 - 20° N latitude range. The temporal
204 evolution of the TEC for a few satellites is shown in Figure 5 (b). Mean TEC and its change
205 index i.e. ROTI is shown in Figure 5 (c). Of our interest is G28's TEC measurement as its
206 IPPs trajectory lay close to the imager's ROI1 during 1700-1800 UT which showed a strong
207 signature of GWs. By performing the periodogram analysis of the temporal and spatial
208 variation of its TEC, we estimated the propagation characteristics of GW to be $\tau \sim 0.95 \pm 0.03$
209 h, $\lambda \sim 229 \pm 12$ km, and $v \sim 67 \pm 5$ m/s, and is in good agreement with the ASAI observations.
210 Further, the propagation direction of GWs seen in airglow imaging is in good agreement with
211 these previous reports. Studies on the GW activity at the MLT heights over a farther low-
212 latitude station Prayagraj (25.5° N, formerly Allahabad) in India showed their propagation
213 either northward or northeast around midnight during April-May (Mukherjee et al., 2010). A
214 comprehensive study of thermospheric GWs in the ASAI observations over Tirunelveli (8.7°
215 N) in India during 2013-2015 indicated their propagation toward the north-northwest during
216 the equinoxes (Sau et al., 2018).

217

218 **3.2 GWs-driven revival of fossil depletions**

219 During 1730-1748 UT, faint signatures of depletion DP1 that revived were seen in the ROI1.
220 Depletion DP1 lacked any poleward growth during 1730-1806 UT. Using the equation given
221 in Kelley (2009) and by tracking the poleward tip of depletion, we estimated the apex height

222 of the associated geomagnetic flux tubes (A_H) and found it to be steady at ~ 600 km. Within it,
223 the level of intensity reduction with respect to that of the ambient region (i.e., $\Delta I/I_{\text{ambient region}}$)
224 was $\sim 17\%$. However, depletion DP1 drifted gradually to the east with a speed of 59-70 m/s.
225 Beginning 1812-1818 UT, this depletion started to intensify steadily, gain contrast against the
226 background and become noticeable. Southern end of depletion DP1 was fused with that of a
227 preceding depletion OD2. A few faint NS-aligned depletions were also present in the ROI1.
228 Along with depletion DP1, they intersected the EW-aligned fronts 'f1' and 'f2' of GWs, and
229 fragmented them into few isolated structures. Later on, these structures got attached to the
230 west wall of depletion DP1 and started moving in unison. Clear signs of two such fragments
231 (marked as S1 and S2 in Figure 1 and 2) can be seen at ~ 1830 UT and ~ 1806 -1812 UT,
232 respectively. Starting 1824-1830 UT, we noted airglow enhancement to occur near its east
233 wall that then started to become distinct. As a result, an *inverted arrowhead*-shaped depletion
234 with an unusually wide southern fraction was evident during 1836-1854 UT. As two attached
235 structures S1 and S2 drifted along with depletion DP1, they tilted considerably to the east by
236 ~ 60 - 75° (see the ASAI images beginning 1830 UT in Figures 1 and 2). At ~ 1900 UT, the
237 structure S1 was almost aligned and merged with the west wall of depletion DP1, which led
238 to a fairly distinct west wall (seen as weak airglow enhancement). Airglow enhancement near
239 both the east and west wall (marked as A1 and A2, respectively, in Figure 2) continued, and a
240 linear NS-aligned depletion DP1 (having $A_H > 800$ km and $\Delta I/I_{\text{ambient region}} \sim 50\%$) was seen at
241 1906-1912 UT. Within the next 6-12 min, the apex of structure S2 merged with airglow
242 enhancement A2 near the west wall.

243

244 Next, some airglow enhancement occurred in the inner edge of the west wall of depletion
245 DP1 at 1924 UT (see the region-of-interest, ROI2 in Figure 2). We interpret this as a
246 consequence of some ambient plasma intrusion across its west wall. Later, such intrusion led
247 to the disappearance of its southern fraction and the formation of an isolated depletion at
248 1942 UT. Possibly these disappearances occurred due to the filling of the EIA plasma into
249 depletion across its western wall (see Otsuka et al., 2012). Similarly, fossil depletion DP2
250 also revived; however, its evolution was much simpler than that of depletion DP1.

251

252 **4 Discussions**

253 We present rare simultaneous observations of GWs activity and associated revival of fossil
254 depletions in the F-region airglow imaging around midnight over an off-equatorial station

255 Ranchi (located near the EIA crest) in India. Post-sunset ionospheric irregularities, in the
256 equatorial region, are generated by the GRT instability that sets off under the suitable
257 combination of (i) favourable alignment of solar terminator with geomagnetic field lines; (ii)
258 rapid height rise of the F-layer; (iii) absence of strong transequatorial wind and (iv) necessary
259 seed perturbation (Fejer and Kelley, 1980; Kelley, 2009; Makela and Otsuka, 2012;
260 Woodman, 2009). Stronger the height rise of the F-layer and an initial seed perturbation is,
261 the faster the growth rate of GRT instability, which ultimately leads to the rapid evolution of
262 the irregularities (Huba and Joyce, 2007; Huang et al., 1993; Hysell et al., 2014; Kelley et al.,
263 1981; Krall et al., 2013; Tsunoda, 2010; Zalesak and Ossakow, 1980). GWs are well known
264 to deform the bottom side plasma of the F-region into the wavelike ionization structures that
265 then act as a seed to GRT instability, which, in turn, generates irregularities (Kelley et al.,
266 1981; Hysell et al., 1990; Huba and Liu, 2020). While their role in the generation of the post-
267 sunset irregularities is well known, our understanding is limited in the context of
268 midnight/post-midnight irregularities. Present study features midnight fossil airglow
269 depletions that revived due to undergoing GW activity and turned into an active depletion.

270

271 Northward propagating GWs having $\lambda \sim 210$ km, $v \sim 64$ m/s, and $\tau \sim 0.91$ h were recorded in
272 630 nm nightglow images during 1715-1906 UT. Supporting airglow observations, TEC
273 measurements, too, showed the presence of similar GWs. Simultaneously, an eastward
274 drifting fossil depletion DP1 ($A_H \sim 600$ km and $\Delta I/I_{\text{ambient region}} \sim 17\%$) co-existed during
275 1730-1748 UT. Next, depletion DP1 and other co-existing depletions intercepted EW-aligned
276 GW fronts and fragmented them during 1806-1824 UT. Subsequently, two such fragments
277 viz. S1 and S2 that lay close to depletion DP1 got attached to its west wall, started drifting
278 eastward in unison, tilted significantly to the east, and almost got aligned with the west wall.
279 Next, depletion DP1 gradually intensified, surged polewards, and became a well-developed
280 linear depletion ($A_H > 800$ km and $\Delta I/I_{\text{ambient region}} \sim 50\%$) during 1906-1912 UT. Meanwhile,
281 airglow enhancement continued to develop near both its walls and an uneven broadening was
282 seen in its southern half. Next, some ambient plasma diffusion occurred near this uneven
283 region leading to airglow enhancement in the inner edge of its west wall at 1924 UT. Such
284 intrusion continued, its southern fraction gradually disappeared, and an isolated depletion was
285 formed at 1942 UT. Present observations clearly indicate that “fossil depletion” DP1 revived
286 and became an “active depletion” under the influence of co-existing GWs activity. Another
287 succeeding depletion, DP2, too, showed a similar revival.

288

289 An important consideration in the GWs seeding of the GRT instability is the alignment of
290 their wavefronts with the geomagnetic field lines. The current understanding is that the
291 strength of the polarization electric field generated by the GWs greatly depends on the angle
292 between them, and the maximum polarization occurs when their wavefront is aligned with the
293 geomagnetic field (Huba et al., 2015; Hysell et al., 2014; Krall et al., 2013; Tulasi Ram et al.,
294 2014; Tsunoda, 2010). Numerical simulations by Hysell et al. (2014) suggest that the GWs-
295 induced modulations were the most severe when their fronts were aligned with the magnetic
296 meridian. Using Communications/Navigation Outrage Forecasting System (C/NOFS) mission
297 TEC measurements, Tulasi Ram et al. (2014) studied the characteristics of large-scale wave
298 structure (LSWS) at the base of the F-region and their association with the EPBs occurrences
299 in Southeast Asia and Africa. Authors found that the EPBs frequently occurred when the
300 amplitudes of LSWS were adequately increased, and their phase fronts were geomagnetic
301 field-aligned.

302

303 In the present study, the GWs fronts were east-west aligned (i.e., transverse to the
304 geomagnetic field lines) and propagated northward. Yet, fossil depletions DP1 and DP2
305 revived and is intriguing. Meridional wind perturbations associated with GWs are known to
306 be ineffective in the initiation and development of depletions. Present observations are in
307 contrast with this notion and point towards another excitation mechanism rather than GRT
308 instability, which we conjecture, is the spatial resonance mechanism for these reasons. Good
309 matching was seen between the GWs phase speed ($v \sim 64-67$ m/s) and the eastward drift of
310 depletion DP1 ($v \sim 59-70$ m/s). Horizontal Wind Model 2007 estimates also indicated the
311 zonal thermospheric wind speed of 51-61 m/s (Drob et al., 2008). We estimated the speed at
312 which the apex of DP1 progressed poleward and found it to be in the range of 46-56 m/s.
313 Spatial resonance theory of GWs seeding of irregularities states that the effects of GWs
314 perturbations are the strongest when its phase speed and the plasma drift velocity are nearly
315 equal (Kelley et al., 1981). Under such conditions, the ionospheric plasma exerts the GW-
316 associated forcing for a longer duration; thereby, accelerating the formation of ionization
317 structures. As such, we conjecture that this GWs-driven revival of fossil depletions occurred
318 via the spatial resonance mechanism. Numerical simulations by Huang and Kelley (1996)
319 suggest that this mechanism can accelerate the formation of depletions. Possibly continuously
320 undergoing GWs activity for 2 hours in the F-region sufficiently intensified the magnitude of

321 associated ionization modulations, which in turn triggered and sustained the revival of fossil
322 depletions via the spatially resonant mechanism.

323

324 Similar event of GWs associated revival of a fossil depletion occurred around midnight on 06
325 March 2013 as well and is shown in Figure 6. On this night, GW activity persisted during
326 1530-1745 UT and concerned fossil depletion **DP3** revived during 1730-1854 UT. Typical
327 ASAI images showing the signs of GW activity are presented in Figure 7. During 1636-1736
328 UT, GWs had $\lambda \sim 196 \pm 4$ km, $v \sim 160 \pm 4$ m/s and $\tau \sim 0.34 \pm 0.02$ h, propagated from SW-
329 NE, and their fronts were $\sim 74^\circ$ aligned with the geomagnetic field line. First, the southern
330 fraction of depletion **DP3** drifted into the western edge of the FOV at 1706-1712 UT. Later,
331 this depletion was seen as an isolated linear depletion during 1730-1736 UT confined within
332 the ~ 20.1 - 23.2° N latitude regime with NS extension of $\sim 480 \pm 18$ km. On course of its
333 eastward drift, depletion **DP3** gradually intensified and developed both poleward and
334 equatorward. During 1706-1800 UT, its base swiftly surged equatorward approximately from
335 20.2° to 17.7° N. Comparatively, its poleward growth was slower. When well-developed at
336 1900 UT, its NS extension was in 17 - 26° N latitudes (i.e. greater than 980 ± 22 km).
337 Simultaneously, two structuring **BR1** and **BR2** developed on its east wall and an isolated
338 depletion (**ID1**) lay on its east at $\sim 20.5^\circ$ N latitude. We found its drift speed to be in the 81-
339 109 m/s range.

340

341 Meridional wind can influence the growth rate of GRT instability by altering the field-line
342 integrated Pederson conductivity. Maruyama (1988) and Abdu et al. (2006) found that strong
343 meridional winds could reduce the growth rate of RTI and suppress irregularities. Huba and
344 Krall (2013) have reported both stabilizing and destabilizing effects of the meridional winds
345 on RT instability. Devasia et al. (2002) found that a suitable combination of the meridional
346 wind and F-region base height favours ESF development. In the present study, the meridional
347 wind measurements using a Fabry-Perot interferometer, etc. were not available; hence, their
348 possible role in the evolution of these fossil depletions could not be investigated.

349

350 We know that the electric field perturbations associated with MSTIDs can influence the
351 growth of irregularities. Otsuka et al. (2012) and Shiokawa et al. (2015) reported the
352 disappearance of an EPB upon interaction with MSTIDs and large-scale traveling ionospheric
353 disturbances (LSTIDs), respectively. Authors suggested that the electric field associated with

354 MSTIDs/LSTIDs can move ambient plasma into the bubble across the geomagnetic field line
355 through $\mathbf{E} \times \mathbf{B}$ drift which will result in the filling and subsequent disappearance of the
356 depletion. Studies by Miller et al. (2009), Taori et al. (2015) and Takahashi et al. (2020)
357 suggest that MSTIDs can directly seed EPBs. Simulation studies by Krall et al. (2011),
358 further, indicates that the electric field associated with electrified MSTIDs can enhance the
359 growth of EPBs. Lately, Wrasse et al. (2021) presented an interesting observations of the
360 interaction of a fossil EPB with an electrified MSTID over 13.3° S. After interaction with the
361 MSTID, concerned fossil EPB merged with other four EPBs, developed poleward and
362 bifurcated. Using detrended TEC data, Takahashi et al. (2021) studied the LSWS over Latin
363 America and found them to be effective in seeding EPBs.

364

365 **5 Summary**

366 We present, here, airglow imaging observations of fossil plasma depletions that revived
367 afresh under the action of prolonged GW activity and became active depletions. Such
368 simultaneous imaging of thermospheric GWs and depletions was recorded in the ASAI of OI
369 630 nm emission over Ranchi (mlat. $\sim 19^\circ$ N), India, on 16 April 2012. Salient features of the
370 present study are as under:

- 371 1. First, airglow images showed EW-aligned and SN-propagating GWs ($\lambda \sim 210$ km, v
372 ~ 64 m/s, and $\tau \sim 0.91$ h) over Ranchi during 1715-1906 UT. Similar GWs were, also,
373 seen in TEC measurements over a lower latitude station Hyderabad.
- 374 2. A co-existing and prominent fossil depletion DP1 revived under this GW activity
375 wherein its apex raised from 600 km to >800 km, and the level of intensity depletion
376 increased from 17 % to 50 %. Another fossil depletion DP2, too, revived.
377 Interestingly, GWs phase fronts were transverse to the geomagnetic field lines, yet
378 two fossil depletions revived under their influence and became active depletions.
- 379 3. As GWs phase speed ($v \sim 64$ -67 m/s) nearly matched the eastward drift of depletion
380 DP1 ($v \sim 59$ -70 m/s), we conjecture that the GWs-driven revival of these fossil
381 depletions possibly occurred via the spatial resonance mechanism.
- 382 4. An uneven region of increased thickness existed on the southern half of the revived
383 depletion DP1, wherein some airglow enhancement was seen later in the inner edge of
384 its west wall. Possibly the gradual disappearance of its southern fraction occurred
385 because of the intrusion of ambient plasma across the west wall.

386

387 Contrary to the current understanding, this study shows that the GWs fronts aligned
388 perpendicular to the geomagnetic field lines can effectively grow irregularities. Present
389 observations of the GWs-driven revival of fossil airglow depletions further contribute to our
390 understanding of their generation mechanism around midnight.

391

392

393 **Data Availability.** Airglow data used in the present study are available through the
394 institutional data repository (<http://www.iigm.res.in/>) or
395 <https://doi.org/10.5281/zenodo.8143215>. Movie created from all-sky 630 nm nightglow
396 images showing the gravity wave activity and the evolution of depletion DP1 and DP2 is
397 available from <https://doi.org/10.5281/zenodo.8358134>. Calibrated TEC data is available
398 from <https://t-ict4d.ictp.it/nequick2/gnss-tec-calibration>.

399

400

401 **Author contributions.** NP conceptualized the research problem and prepared the first draft.
402 All authors contributed to the interpretation of results, discussion, and subsequent drafting of
403 the manuscript.

404

405

406 **Acknowledgements:** Funds for Airglow Research at *Indian Institute of Geomagnetism* are
407 being provided by *Department of Science and Technology (DST), Govt. of India, New*
408 *Delhi*. GNSS TEC Calibrated data were downloaded from [https://t-](https://t-ict4d.ictp.it/nequick2/gnss-tec-calibration)
409 [ict4d.ictp.it/nequick2/gnss-tec-calibration](https://t-ict4d.ictp.it/nequick2/gnss-tec-calibration) and *Telecommunications/ICT for Development*
410 *(T/ICT4D) Laboratory of the Abdus Salam International Centre for Theoretical Physics,*
411 *Trieste, Italy* is gratefully acknowledged. *SP* is grateful to *Director, Indian Institute of*
412 *Geomagnetism, Navi Mumbai* for the award of Research Scholarship. Authors sincerely
413 thank the Editor and Reviewers for their encouragement and critical comments.

414

415

416 **Competing interests:** The contact author has declared that none of the authors has any
417 competing interests

418

419 **References:**

420 Abdu, M., Iyer, K. N., de Medeiros, R., Batista, I. S. and Sobral, J. H.: Thermospheric
421 meridional wind control of equatorial spread F and evening prereversal electric field,
422 *Geophys. Res. Lett.* 33 (7). <http://dx.doi.org/10.1029/2005GL024835>, 2006.

423

424 Abdu, M. A., Kherani, E. A., Batista, I. S., de Paula, E. R., Fritts, D. C., and Sobral, J. H.:
425 Gravity wave initiation of equatorial spread F/plasma bubble irregularities based on
426 observational data from the SpreadFEx campaign, *Ann. Geophys.*, 27, 2607-2622.
427 <https://doi.org/10.5194/angeo-27-2607-2009>, 2009.

428

429 Azeem, I., and Barlage, M.: Atmosphere-ionosphere coupling from convectively generated
430 gravity waves. *Adv. Space Res.*, 61(7), 1931-1941. <https://doi.org/10.1016/j.asr.2017.09.029>,
431 2018.

432

433 Ciraolo, L., Azpilicueta, F., Brunini, C., Meza, A. and Radicella, S. M.: Calibration errors on
434 experimental slant total electron content (TEC) determined with GPS. *J. Geod.*, 81, 111–120,
435 <https://doi.org/10.1007/s00190-006-0093-1>, 2007.

436

437 Chapagain, N. P., Taylor, M. J., and Eccles, J. V.: Airglow observations and modeling of F
438 region depletion zonal velocities over Christmas Island, *J. Geophys. Res.*, 116, A02301,
439 <https://doi.org/10.1029/2010JA015958>, 2011.

440

441 Devasia, C., Jyoti, N., Subbarao, K., Viswanathan, K., Tiwari, D. and Sridharan, R.: On the
442 plausible linkage of thermospheric meridional winds with the equatorial spread F, *J. Atmos.*
443 *Sol.-Terrest. Phys.* 64 (1), 1–12, [http://dx.doi.org/10.1016/S1364-6826\(01\)00089-X](http://dx.doi.org/10.1016/S1364-6826(01)00089-X), 2002.

444

445 Drob, D. P., Emmert, J. T., Crowley, G., Picone, J. M., Shepherd, G. G., Skinner, W., et al.:
446 An empirical model of the Earth's horizontal wind fields: HWM07. *J. Geophys. Res.*, 113,
447 A12304, <https://doi.org/10.1029/2008JA013668>, 2008.

448

449 Fejer, B. G., and Kelley, M. C.: Ionospheric irregularities. *Rev. Geophys.*, 18(2), 401-454,
450 <https://doi.org/10.1029/RG018i002p00401>, 1980.

451

452 Figueiredo, C. A. O. B., Takahashi, H., Wrasse, C. M., Otsuka, Y., Shiokawa, K., & Barros,
453 D.: Medium-scale traveling ionospheric disturbances observed by detrended total electron
454 content maps over Brazil. *Journal of Geophysical Research: Space Physics*, 123, 2215–2227.
455 <https://doi.org/10.1002/2017JA025021>, 2018.

456

457 Ford, E. A. K., Aruliah, A. L., Griffin, E. M., and McWhirter, I.: Thermospheric gravity
458 waves in Fabry-Perot Interferometer measurements of the 630.0nm OI line, *Ann. Geophys.*,
459 24, 555–566, <https://doi.org/10.5194/angeo-24-555-2006>, 2006.

460

461 Ford, E. A. K., Aruliah, A. L., Griffin, E. M., and McWhirter, I.: Statistical analysis of
462 thermospheric gravity waves from Fabry-Perot Interferometer measurements of atomic
463 oxygen, *Ann. Geophys.*, 26, 29–45, <https://doi.org/10.5194/angeo-26-29-2008>, 2008.

464

465 Fritts, D. C., and Alexander, M. J.: Gravity wave dynamics and effects in the middle
466 atmosphere, *Rev. Geophys.*, 41, 1003, <https://doi.org/10.1029/2001RG000106>, 2003.

467

468 Fritts, D. C., Abdu, M. A., Batista, B. R., Batista, I. S., Batista, P. P., Buriti, R., Clemesha, B.
469 R., Dautermann, T., de Paula, E. R., Fechine, B. J., Fejer, B. G., Gobbi, D., Haase, J.,
470 Kamalabadi, F., Kherani, E. A., Laughman, B., Lima, P. P., Liu, H.-L., Medeiros, A., Pautet,
471 P.-D., Riggan, D. M., Rodrigues, F. S., São Sabbas, F., Sobral, J. H. A., Stamus, P.,
472 Takahashi, H., Taylor, M. J., Vadas, S. L., Vargas, F., and Wrasse, C. M.: Overview and
473 summary of the Spread F Experiment (SpreadFEx), *Ann. Geophys.*, 27, 2141–2155,
474 <https://doi.org/10.5194/angeo-27-2141-2009>, 2009.

475

476 Fukushima, D., Shiokawa, K., Otsuka, Y., and Ogawa, T.: Observation of equatorial
477 nighttime medium-scale traveling ionospheric disturbances in 630-nm airglow images over 7
478 years. *J. Geophys. Res.*, 117, A10324. <https://doi.org/10.1029/2012JA017758>, 2012.

479

480 Garcia, F. J., Taylor, M. J., and Kelley, M. C.: Two-dimensional spectra analysis of
481 mesospheric airglow image data. *Appl. Opt.*, 36(29), 7374-7385.
482 <https://doi.org/10.1364/AO.36.007374>, 1997.

483

484 Heale, C. J., Inchin, P. A., and Snively, J. B.: Primary versus secondary gravity wave
485 responses at F-region heights generated by a convective source, *J. Geophys. Res. Space*
486 *Physics*, 127, e2021JA029947, <https://doi.org/10.1029/2021JA029947>, 2022.

487

488 Huang, C.-S., Kelley, M. C., and Hysell, D. L.: Nonlinear Rayleigh-Taylor instabilities,
489 atmospheric gravity waves and equatorial spread F, *J. Geophys. Res.*, 98(A9), 15631-15642,
490 <https://doi.org/10.1029/93JA00762>, 1993.

491

492 Huang, C.-S., and Kelley, M. C.: Nonlinear evolution of equatorial spread F: 1. On the role of
493 plasma instabilities and spatial resonance associated with gravity wave seeding, *J. Geophys.*
494 *Res.*, 101(A1), 283-292, <https://doi.org/10.1029/95JA02211>, 1996.

495

496 Huba, J. D., and Joyce, G.: Equatorial spread F modeling: Multiple bifurcated structures,
497 secondary instabilities, large density ‘bite-outs’ and supersonic flows. *Geophys. Res. Lett.*,
498 34, L07105. <https://doi.org/10.1029/2006GL028519>, 2007.

499

500 Huba, J. D., Joyce, G., and Krall, J.: Three-dimensional equatorial spread F modeling,
501 *Geophys. Res. Lett.*, 35, L10102. <https://doi.org/10.1029/2008GL033509>, 2008.

502

503 Huba, J. D., and Joyce, G.: Global modeling of equatorial plasma bubbles, *Geophys. Res.*
504 *Lett.*, 37, L17104, <https://doi.org/10.1029/2010GL044281>, 2010.

505

506 Huba, J. D., and Krall, J.: Impact of meridional winds on equatorial spread F: Revisited,
507 *Geophys. Res. Lett.*, 40, 1268– 1272, doi:10.1002/grl.50292, 2013.

508

509 Huba, J. D., Drob, D. P., Wu, T.-W., and Makela, J. J.: Modeling the ionospheric impact of
510 tsunami-driven gravity waves with SAMI3: Conjugate effects. *Geophys. Res. Lett.*, 42,
511 5719–5726. <https://doi.org/10.1002/2015GL064871>, 2015.

512

513 Huba, J. D., and Liu, H.-L.: Global modeling of equatorial spread F with SAMI3/WACCM-
514 X. *Geophys. Res. Lett.*, 47, e2020GL088258. <https://doi.org/10.1029/2020GL088258>, 2020.

515

516 Hysell, D. L., Kelley, M. C., Swartz, W. E., and Woodman, R. F.: Seeding and layering of
517 equatorial spread F by gravity waves. *J. Geophys. Res.*, 95(A10), 17,253-17,260.
518 <https://doi.org/10.1029/JA095iA10p17253>, 1990.

519

520 Hysell, D. L., Jafari, R., Fritts, D. C., and Laughman, B.: Gravity wave effects on postsunset
521 equatorial F region stability, *J. Geophys. Res. Space Physics*, 119, 5847– 5860,
522 doi:10.1002/2014JA019990, 2014.

523

524 Kelley, M. C., Larsen, M. F., LaHoz, C., and McClure, J. P.: Gravity wave initiation of
525 equatorial spread F: A case study, *J. Geophys. Res.*, 86 (A11), 9087-9100,
526 <https://doi.org/10.1029/JA086iA11p09087>, 1981.

527

528 Kelley, M. C.: *The Earth's ionosphere: Plasma physics and electrodynamics* (2nd ed.).
529 Burlington, MA: Elsevier, 2009.

530

531 Klausner, V., Fagundes, P. R., Sahai, Y., Wrasse, C. M., Pillat, V. G., and Becker-Guedes, F.:
532 Observations of GW/TID oscillations in the F2 layer at low latitude during high and low solar
533 activity, geomagnetic quiet and disturbed periods, *J. Geophys. Res.*, 114, A02313,
534 <https://doi.org/10.1029/2008JA013448>, 2009.

535

536 Krall, J., Huba, J. D., Ossakow, S. L., Joyce, G., Makela, J. J., Miller, E. S., and Kelley, M.
537 C.: Modeling of equatorial plasma bubbles triggered by non-equatorial traveling ionospheric
538 disturbances. *Geophys. Res. Lett.*, 38(8), L08103. <https://doi.org/10.1029/2011GL046890>,
539 2011.

540

541 Krall, J., Huba, J. D., and Fritts, D. C.: On the seeding of equatorial spread F by gravity
542 waves, *Geophys. Res. Lett.*, 40, 661-664, <https://doi.org/10.1002/grl.50144>, 2013.

543

544 Makela, J. J., Ledvina, B. M., Kelley, M. C. and. Kintner, P. M: Analysis of the seasonal
545 variations of equatorial plasma bubble occurrence observed from Haleakala, Hawaii, *Ann.*
546 *Geophys.*, 22, 3109-3121, <https://doi.org/10.5194/angeo-22-3109-2004>, 2004.

547

548 Makela, J. J., Kelley, M. C., and Nicolls, M. J.: Optical observations of the development of
549 secondary instabilities on the eastern wall of an equatorial plasma bubble. *J. Geophys. Res.*,
550 111, A09311, <https://doi.org/10.1029/2006JA011646>, 2006.
551

552 Makela, J. J., Lognonne, P., Hebert, H., Gehrels, T., Rolland, L., Allgeyer, S., et al.: Imaging
553 and modeling the ionospheric airglow response over Hawaii to the tsunami generated by the
554 Tohoku earthquake of 11 March 2011. *Geophys. Res. Lett.*, 38, L00G02.
555 <https://doi.org/10.1029/2011GL047860>, 2011.
556

557 Makela, J. J., and Otsuka, Y.: Overview of nighttime ionospheric instabilities at low- and
558 mid-latitudes: Coupling aspects resulting in structuring at the mesoscale. *Space Sci. Rev.*,
559 168(1-4), 419-440. <https://doi.org/10.1007/s11214-011-9816-6>, 2012.
560

561 Maruyama, T.: A diagnostic model for equatorial spread F: 1. Model description and
562 application to electric field and neutral wind effects, *J. Geophys. Res.*, 93 (A12), 14611–
563 14622. <http://dx.doi.org/10.1029/JA093iA12p14611>, 1988.
564

565 Maurya, A. K., Parihar, N., Dube, A., Singh, R., Kumar, S., Chanrion, O., Tomicic, M., and
566 Neubert, T.: Rare observations of sprites and gravity waves supporting D, E, F-regions
567 ionospheric coupling, *Sci. Rep.*, 12, 581. <https://doi.org/10.1038/s41598-021-03808-5>, 2022.
568

569 Mendillo, M., and Baumgardner, J.: Airglow characteristics of equatorial plasma depletions.
570 *J. Geophys. Res.*, 87, 7641-7652, <https://doi.org/10.1029/JA087iA09p07641>, 1982.
571

572 Mendillo, M., Baumgardner, J., Colerico, M., and Nottingham, D.: Imaging science
573 contributions to equatorial aeronomy: initial results from the MISETA program, *J. Atmos.*
574 *Terr. Phys.*, 59, 1587-1599, [https://doi.org/10.1016/S1364-6826\(96\)00158-7](https://doi.org/10.1016/S1364-6826(96)00158-7), 1997.
575

576 Miller, E. S., Makela, J. J., and Kelley, M. C.: Seeding of equatorial plasma depletions by
577 polarization electric fields from middle latitudes: Experimental evidence, *Geophys. Res.*
578 *Lett.*, 36, L18105, <https://doi.org/10.1029/2009GL039695>, 2009.
579

580 Mukherjee, G. K., Pragati Shikha, R., Parihar, N., Ghodpage, R. and Patil, P. T.: Studies of
581 the wind filtering effect of gravity waves observed at Allahabad (25.45° N, 81.85° E). *Earth*
582 *Planets Space* 62, 309-318, <https://doi.org/10.5047/eps.2009.11.008>, 2010.

583

584 Nishioka, M., Otsuka, Y., Shiokawa, K., Tsugawa, T., Effendy, , Supnithi, P., Nagatsuma, T.,
585 and Murata, K. T.: On post-midnight field-aligned irregularities observed with a 30.8-MHz
586 radar at a low latitude: Comparison with F-layer altitude near the geomagnetic equator, *J.*
587 *Geophys. Res.*, 117, A08337, <https://doi.org/10.1029/2012JA017692>, 2012.

588

589 Otsuka, Y., Shiokawa, K. and Ogawa, T.: Disappearance of equatorial plasma bubble after
590 interaction with mid-latitude medium-scale traveling ionospheric disturbance, *Geophysical*
591 *Research Letters*, 39, L14105, <https://doi.org/10.1029/2012GL052286>, 2012.

592

593 Otsuka, Y.: Review of the generation mechanisms of post-midnight irregularities in the
594 equatorial and low-latitude ionosphere. *Prog.. Earth Planet. Sci.* 5, 57.
595 <https://doi.org/10.1186/s40645-018-0212-7>, 2018.

596

597 Parihar, N., Singh, D., and Gurubaran, S.: A comparison of ground-based hydroxyl airglow
598 temperatures with SABER/TIMED measurements over 23° N, India, *Ann. Geophys.*, 35,
599 353–363, <https://doi.org/10.5194/angeo-35-353-2017>, 2017.

600

601 Parihar, N., Radicella, S. M., Nava, B., Migoya-Orue, Y. O., Tiwari, P., and Singh, R.: An
602 investigation of the ionospheric F region near the EIA crest in India using OI 777.4 and 630.0
603 nm nightglow observations. *Ann. Geophys.*, 36(3), 809-823. [https://doi.org/10.5194/angeo-](https://doi.org/10.5194/angeo-36-809-2018)
604 [36-809-2018](https://doi.org/10.5194/angeo-36-809-2018), 2018.

605

606 Parihar, N.: Rare occurrence of off-equatorial edge initiating and equatorward surging plasma
607 depletions observed in OI 630-nm imaging. *J. Geophys. Res. Space Physics*, 124, 2887-2896.
608 <https://doi.org/10.1029/2018JA026155>, 2019.

609

610 Paulino, I., Takahashi, H., Medeiros, A. F., Wrasse, C. M., Buriti, R. A., Sobral, J. H. A., and
611 Gobbi, D.: Mesospheric gravity waves and ionospheric plasma bubbles observed during the
612 COPEX campaign. *J. Atmos. Sol.-Terr. Phys.*, 73(11-12), 1575-1580.
613 <https://doi.org/10.1016/j.jastp.2010.12.004>, 2011.

614

615 Paulino, I., Medeiros, A. F., Vadas, S. L., Wrasse, C. M., Takahashi, H., Buriti, R. A., Leite,
616 D., Filgueira, S., Bageston, J. V., Sobral, J. H. A., and Gobbi, D.: Periodic waves in the lower
617 thermosphere observed by OI630 nm airglow images, *Ann. Geophys.*, 34, 293-301,
618 <https://doi.org/10.5194/angeo-34-293-2016>, 2016.

619

620 Paulino, I., Moraes, J. F., Maranhão, G. L., Wrasse, C. M., Buriti, R. A., Medeiros, A. F.,
621 Paulino, A. R., Takahashi, H., Makela, J. J., Meriwether, J. W., and Campos, J. A. V.:
622 Intrinsic parameters of periodic waves observed in the OI6300 airglow layer over the
623 Brazilian equatorial region, *Ann. Geophys.*, 36, 265–273, [https://doi.org/10.5194/angeo-36-](https://doi.org/10.5194/angeo-36-265-2018)
624 [265-2018](https://doi.org/10.5194/angeo-36-265-2018), 2018.

625

626 Pimenta, A. A., Fagundes, P. R., Sahai, Y., Bittencourt, J. A., and Abalde, J. R.: Equatorial F-
627 region plasma depletion drifts: latitudinal and seasonal variations. *Ann. Geophys.*, 21, 2315-
628 2322, <https://doi.org/10.5194/angeo-21-2315-2003>, 2003.

629

630 Sau, S., Narayanan, V. L., Gurubaran, S., and Emperumal, K.: Study of wave signatures
631 observed in thermospheric airglow imaging over the dip equatorial region. *Adv. Space Res.*,
632 62(7), 1762–1774, <https://doi.org/10.1016/j.asr.2018.06.039>, 2018.

633

634 Sekar, R., Chakrabarty, D., Sarkhel, S., Patra, A. K., Devasia, C. V., and Kelley, M. C.:
635 Identification of active fossil bubbles based on coordinated VHF radar and airglow
636 measurements, *Ann. Geophys.*, 25, 2099-2102, <https://doi.org/10.5194/angeo-25-2099-2007>,
637 2007.

638

639 Shiokawa, K., Otsuka, Y., Lynn, K. J., Wilkinson, P., and Tsugawa, T.: Airglow-imaging
640 observation of plasma bubble disappearance at geomagnetically conjugate points. *Earth*
641 *Planets and Space*, 67(1), 43, <https://doi.org/10.1186/s40623-015-0202-6>, 2015.

642

643 Singh, S., Johnson, F. S., and Power, R. A.: Gravity wave seeding of equatorial plasma
644 bubbles. *J. Geophys. Res.*, 102(A4), 7399–7410, <https://doi.org/10.1029/96JA03998>, 1997.

645

646 Smith, S. M., Martinis, C. R., Baumgardner, J., and Mendillo, M.: All-sky imaging of
647 transglobal thermospheric gravity waves generated by the March 2011 Tohoku Earthquake, *J.*

648 Geophys. Res. Space Physics, 120, 10,992-10,999, <https://doi.org/10.1002/2015JA021638>,
649 2015.
650
651 Sreeja, V., Vineeth, C., Pant, T. K., Ravindran, S. and Sridharan, R.: Role of gravity wavelike
652 seed perturbations on the triggering of ESF-First results from unique dayglow observations,
653 Ann. Geophys., 27, 313-318, <https://doi.org/10.5194/angeo-27-313-2009>, 2009.
654
655 Takahashi, H., Taylor, M. J., Pautet, P.-D., Medeiros, A. F., Gobbi, D., Wrasse, C. M.,
656 Fechine, J., Abdu, M. A., Batista, I. S., Paula, E., Sobral, J. H. A., Arruda, D., Vadas, S. L.,
657 Sabbas, F. S., and Fritts, D. C.: Simultaneous observation of ionospheric plasma bubbles and
658 mesospheric gravity waves during the SpreadFEx Campaign, Ann. Geophys., 27, 1477-1487,
659 <https://doi.org/10.5194/angeo-27-1477-2009>, 2009.
660
661 Takahashi, H., Wrasse, C. M., Figueiredo, C. A. O. B., Barros, D., Paulino, I., Essien, P., et
662 al.: Equatorial plasma bubble occurrence under propagation of MSTID and MLT gravity
663 waves. J. Geophys. Res.: Space Physics, 125, e2019JA027566.
664 <https://doi.org/10.1029/2019JA027566>, 2020.
665
666 Takahashi, H., Essien, P., Figueiredo, C. A. O. B., Wrasse, C. M., Barros, D., Abdu, M. A.,
667 Otsuka, Y., Shiokawa, K., and Li, G. Z.: Multi-instrument study of longitudinal wave
668 structures for plasma bubble seeding in the equatorial ionosphere. Earth Planet. Phys., 5(5),
669 368–377. <https://doi.org/10.26464/epp2021047>, 2021.
670
671 Taori, A., Makela, J. J., and Taylor, M. J.: Mesospheric wave signatures and equatorial
672 plasma bubbles: A case study, J. Geophys. Res., 115, A6, A06302,
673 <https://doi.org/10.1029/2009JA015088>, 2010.
674
675 Taori, A., Jayaraman, A., and Kamalakar, V.: Imaging of mesosphere-thermosphere airglow
676 emissions over Gadanki (13.5° N, 79.2° E): First results. J. Atmos. Sol.-Terr. Phys., 93, 21-
677 28. <https://doi.org/10.1016/j.jastp.2012.11.007>, 2013.
678
679 Taori, A., Parihar, N., Ghodpage, R., Dashora, N., Sripathi, S., Kherani, E. A., and Patil, P. T.
680 (2015). Probing the possible trigger mechanisms of an equatorial plasma bubble event based

681 on multistation optical data. *J. Geophys. Res. Space Physics*, 120, 8835-8847.
682 <https://doi.org/10.1002/2015JA021541>.
683
684 Tsunoda, R. T.: On seeding equatorial spread F: Circular gravity waves, *Geophys. Res. Lett.*,
685 37, L10104, <https://doi.org/10.1029/2010GL043422>, 2010.
686
687 Tulasi Ram, S., Yamamoto, M., Tsunoda, R. T., Chau, H. D., Hoang, T. L., Dantie, B.,
688 Wassae, M., Yatini, C. Y., Manik, T., and Tsugawa, T.: Characteristics of large-scale wave
689 structure observed from African and Southeast Asian longitudinal sectors, *J. Geophys. Res.*
690 *Space Physics*, 119, 2288-2297, <https://doi.org/10.1002/2013JA019712>, 2014.
691
692 Vadas, S. L., and Azeem, I.: Concentric secondary gravity waves in the thermosphere and
693 ionosphere over the continental United States on 25-26 march 2015 from deep convection. *J.*
694 *Geophys. Res. Space Physics*, 126, e2020JA028275. <https://doi.org/10.1029/2020JA028275>,
695 2021.
696
697 Wrasse, C. M., Figueiredo, C. A. O. B., Barros, D., Takahashi, H., Carrasco, A. J., Vital, L.
698 F. R., Rezende, L. C. A., Egito, F., Rosa, G. M., and Sampaio, A. H. R.: Interaction between
699 Equatorial Plasma Bubbles and a Medium-Scale Traveling Ionospheric Disturbance,
700 observed by OI 630 nm airglow imaging at Bom Jesus de Lapa, Brazil. *Earth Planet. Phys.*,
701 5(5), 397–406. <https://doi.org/10.26464/epp2021045>, 2021.
702
703 Woodman, R. F.: Spread F: An old equatorial aeronomy problem finally resolved? *Ann.*
704 *Geophys.*, 27(5), 1915-1934. <https://doi.org/10.5194/angeo-27-1915-2009>, 2009.
705
706 Yadav, S., Sridharan, R., Sunda, S. and Pant, T. K.: Further refinements to the spatiotemporal
707 forecast model for L-band scintillation based on comparison with C/NOFS observations, *J.*
708 *Geophys. Res. Space Physics*, 122, 5643-5652, <https://doi.org/10.1002/2017JA023869>, 2017.
709
710 Zalesak, S., and Ossakow, S.: Nonlinear equatorial spread F: Spatially large bubbles resulting
711 from large horizontal scale initial perturbations. *J. Geophys. Res.*, 85(A5), 2131-2142.
712 <https://doi.org/10.1029/JA085iA05p02131>, 1980.
713

714 **Figure Captions**

715 **Figure 1.** ASAI images during 1742-1830 UT over Ranchi (23.3° N, 85.3° E, mlat. ~19° N)
716 on 16 April 2012. DP1 is the first fossil plasma depletion that showed GWs driven revival.
717 Depletions OD1 and OD2 preceded depletion DP1. ROI1 is the region-of-interest wherein the
718 south-north propagating GW activity and faint signatures of eastward drifting depletion DP1
719 were seen initially. Some weakly noticeable GWs fronts are 'f1', 'f2' and 'f3' (in
720 succession). 't1' and 't2' are trough that precede fronts 'f1' and 'f2', respectively. Upon
721 interaction with depletions present in ROI1, EW-aligned GW fronts 'f1' and 'f2' fragmented
722 and formed structures 'S1' and 'S2' that, subsequently, got linked to the west wall of
723 depletion DP1 and started moving in unison.

724
725 **Figure 2.** Airglow images showing the subsequent evolution of depletion DP1 during 1836-
726 1942 UT. On course of their eastward motion, structures 'S1' and 'S2' significantly tilted to
727 east, aligned with the west wall of depletion DP1 and contributed to its revival. DP2 is
728 another fossil depletion that showed GWs driven revival. Some noticeable GWs fronts are
729 'f3' and 'f4'. A1 and A2 are two arc-shaped regions of airglow enhancement near the east
730 and west wall of depletion DP1. ROI2 is the region-of-interest wherein ambient plasma
731 diffusion occurred across the west wall of depletions DP1.

732
733 **Figure 3.** Typical time difference ASAI of OI 630 nm emission over Ranchi showing
734 GW activity during 1742–1830 UT. Noticeable trough and crest of few GW fronts (as shown
735 in Figure 1) are marked as 't1' and 't2' and 'f1', 'f2' and 'f3'. 'S1' and 'S2' are fragmented
736 structures as described in Figure 1.

737
738 **Figure 4.** (a)-(b) North-south (NS) keogram along 84.4° E and 85.3° E longitude generated
739 from OI 630 nm images during 1730-1930 UT. Alternating bright and dark intensity
740 striations (i.e. wave traces) can be seen over North. Probably depletions masked GWs
741 features over South, and hence, these wave traces were not seen. Slope of these striations
742 indicates towards the south-north movement of GW fronts. A few clear wave traces that were
743 used to estimate speed of GWs are marked by black arrow as 'b1', 'b2', 'b3' and 'b4'.

744
745 **Figure 5.** (a) Scatter plot of the TEC along the track of IPPs for a few GPS and GLONASS
746 satellites (prefixed as 'G' and 'R', respectively) in the geographic grid of 5-35° N x 65-95° E
747 during 1630-1930 UT on 16 April 2012. PRN numbers of GPS/GLONASS satellites along

748 with the start time at 1700 UT are marked adjacent to the corresponding IPPs trajectory.
749 G28's trajectory lay close to the south-west sector of the ASAI. Imager's field-of-view is
750 shown by dashed quarter circle with its centre at Ranchi. (b) TEC variations of a few
751 GPS/GLONASS satellites showing the presence of GWs activity. (c) Mean TEC and ROTI
752 variation over Hyderabad (17.3° N, 78.6° E, mlat. ~12.0° N, located equatorward of Ranchi).

753

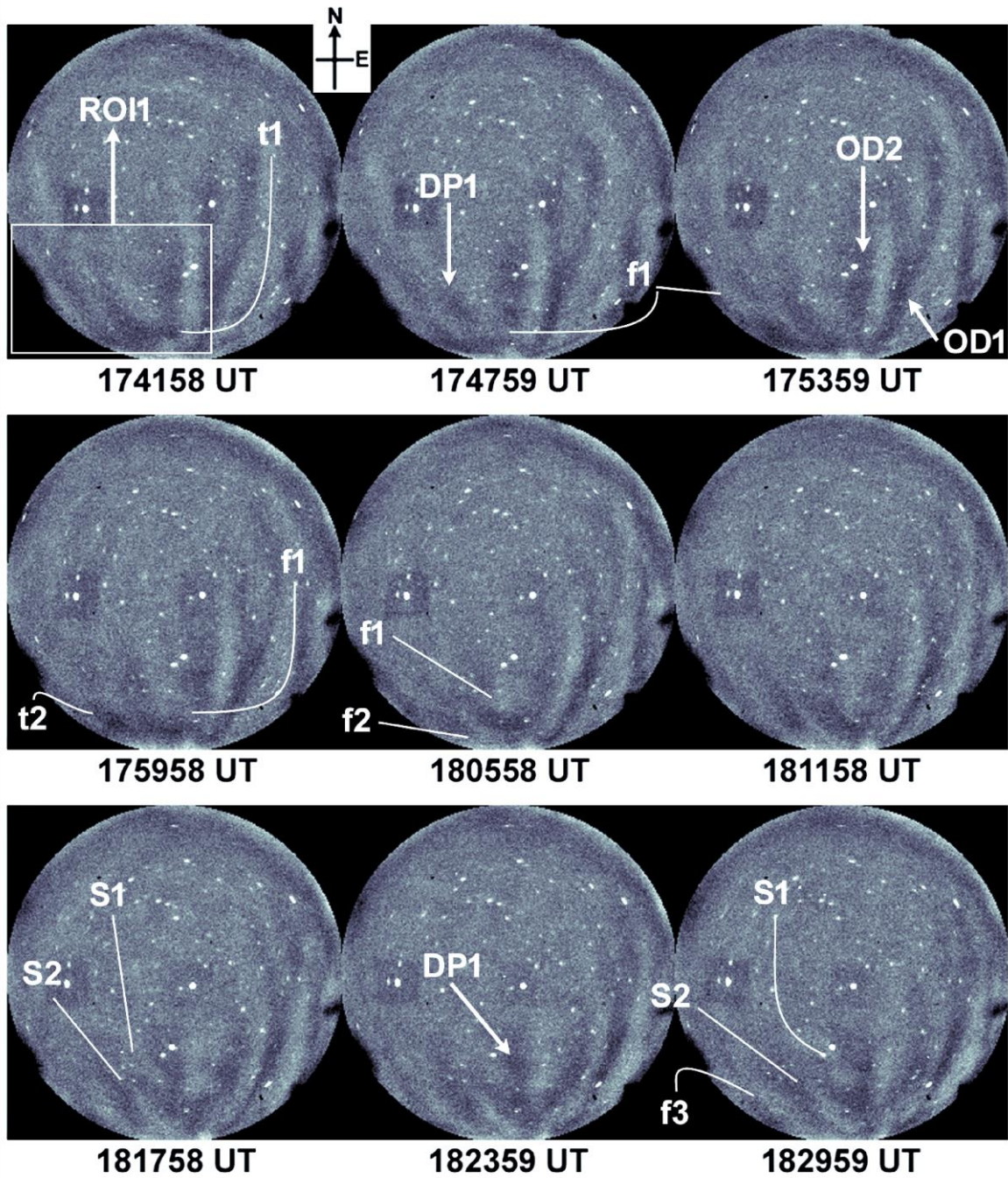
754 **Figure 6.** Selected ASAI images showing the revival of fossil depletion **DP3** during 1730-
755 1854 UT on 06 March 2013 over Ranchi. **ROI3** is the region-of-interest wherein depletion
756 **DP3** appeared sliced by an unclear thin streak of slightly enhanced airglow. **BR1** and **BR2**
757 are two structuring that developed on its east wall.

758

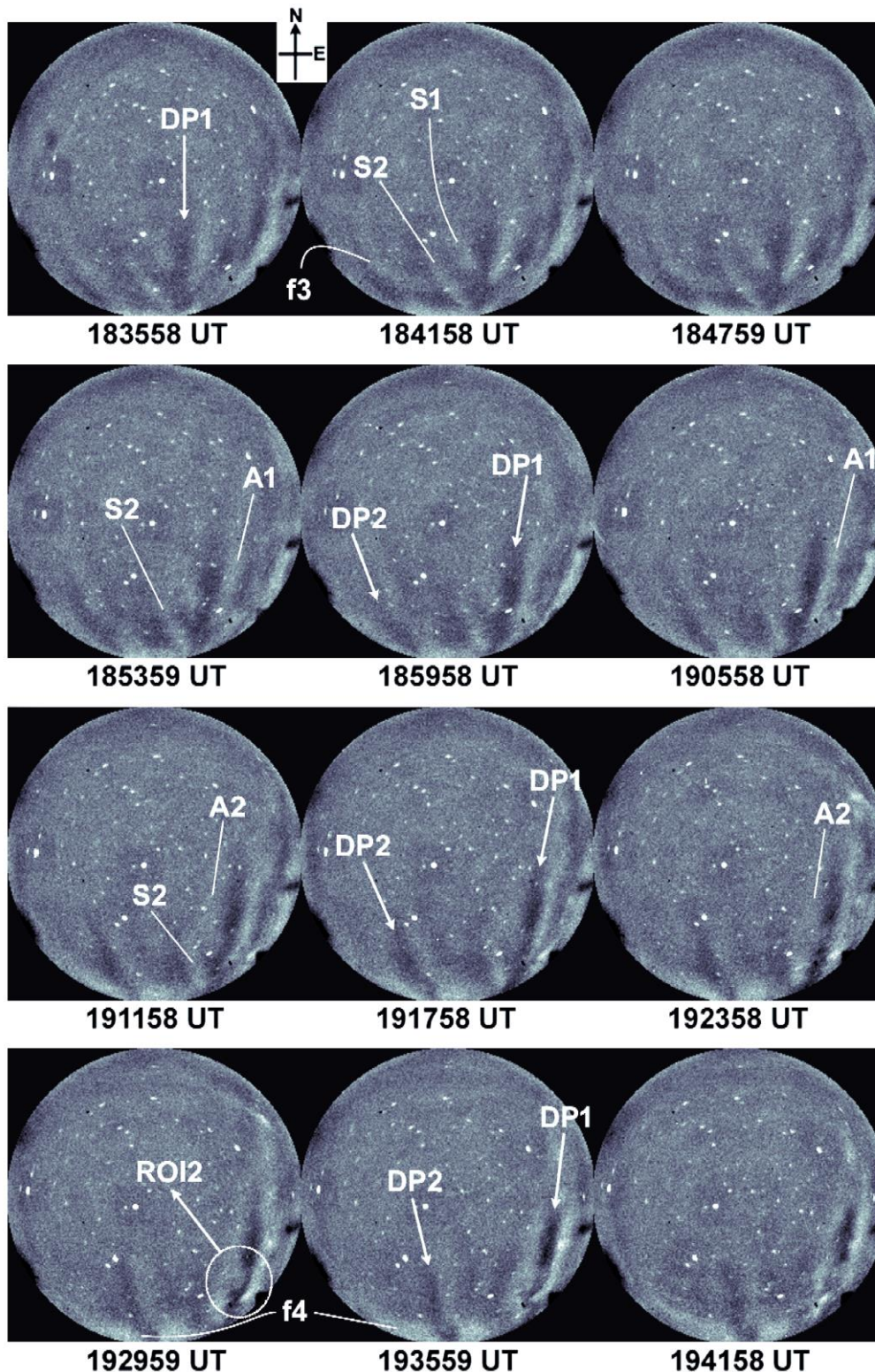
759 **Figure 7.** Limited time difference ASAI images showing GW activity during 1530-1700 UT
760 on 06 March 2013. Beginning 1336 UT, GW signatures were seen in airglow images;
761 however, activity intensified during 1530-1736 UT. Some of clear GW fronts are marked as
762 'g1', 'h1' and 'k1'.

763

764



765
 766 **Figure 1.** ASAI images during 1742-1830 UT over Ranchi (23.3° N, 85.3° E, mlat. ~19° N)
 767 on 16 April 2012. DP1 is the first fossil plasma depletion that showed GWs driven revival.
 768 Depletions OD1 and OD2 preceded depletion DP1. ROI1 is the region-of-interest wherein the
 769 south-north propagating GW activity and faint signatures of eastward drifting depletion DP1
 770 were seen initially. Some weakly noticeable GWs fronts are 'f1', 'f2' and 'f3' (in
 771 succession). 't1' and 't2' are trough that precede fronts 'f1' and 'f2', respectively. Upon
 772 interaction with depletions present in ROI1, EW-aligned GW fronts 'f1' and 'f2' fragmented
 773 and formed structures 'S1' and 'S2' that, subsequently, got linked to the west wall of
 774 depletion DP1 and started moving in unison.



775

776

777

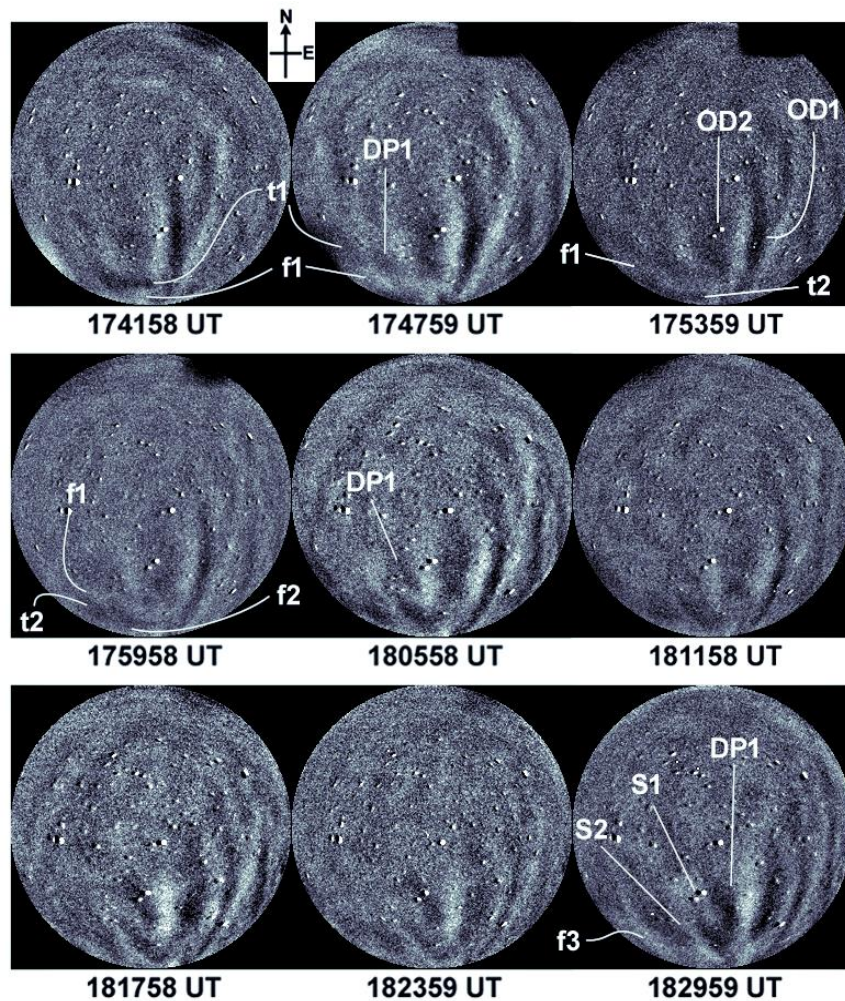
778

779

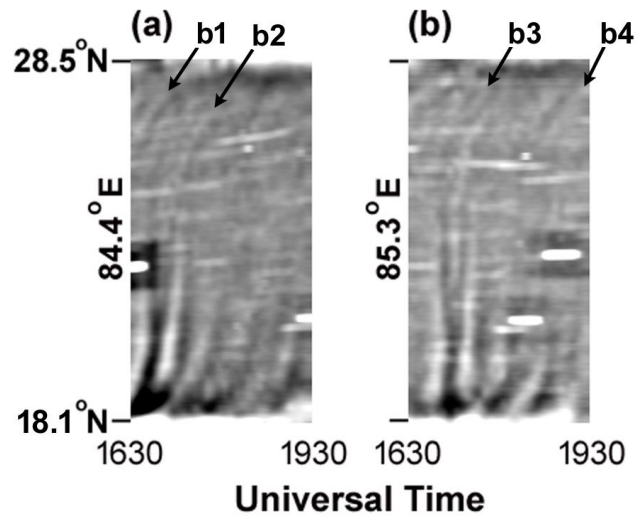
780

Figure 2. Airglow images showing the subsequent evolution of depletion DP1 during 1836-1942 UT. On course of their eastward motion, structures ‘S1’ and ‘S2’ significantly tilted to east, aligned with the west wall of depletion DP1 and contributed to its revival. DP2 is another fossil depletion that showed GWs driven revival. Some noticeable GWs fronts are ‘f3’ and ‘f4’. A1 and A2 are two arc-shaped regions of airglow enhancement near the east

781 and west wall of depletion DP1. ROI2 is the region-of-interest wherein ambient plasma
 782 diffusion occurred across the west wall of depletions DP1. Some noticeable GW fronts are
 783 'f3' and 'f4'. A1 and A2 are two arc-shaped regions of airglow enhancement near the east
 784 and west wall of depletion DP1. ROI2 is the region-of-interest wherein ambient plasma
 785 diffusion occurred across the west wall of depletions DP1.
 786



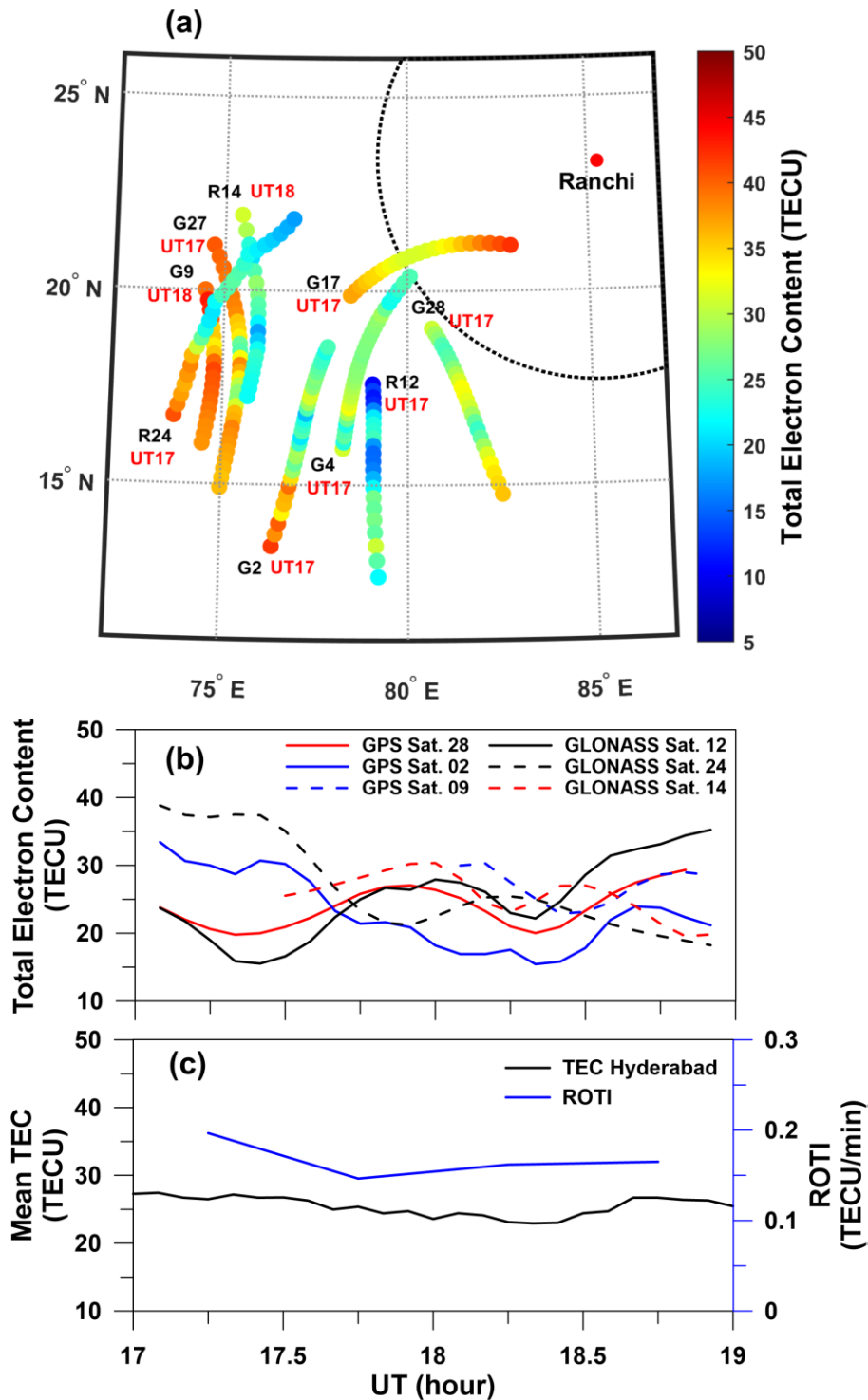
787
 788 **Figure 3.** Typical time difference ASAI of OI 630 nm emission over Ranchi showing GW
 789 activity during 1742–1830 UT. Noticeable trough and crest of few GW fronts (as
 790 shown in Figure 1) are marked as 't1' and 't2' and 'f1', 'f2' and 'f3'. 'S1' and
 791 'S2' are fragmented structures as described in Figure 1.



792

793 **Figure 4.** (a)-(b) North-south (NS) keogram along 84.4° E and 85.3° E longitude generated
 794 from OI 630 nm images during 1730-1930 UT. Alternating bright and dark intensity
 795 striations (i.e. wave traces) can be seen over North. Probably depletions masked GWs
 796 features over South, and hence, these wave traces were not seen. Slope of these striations
 797 indicates towards the south-north movement of GW fronts. A few clear wave traces that were
 798 used to estimate speed of GWs are marked by black arrow as 'b1', 'b2', 'b3' and 'b4'.

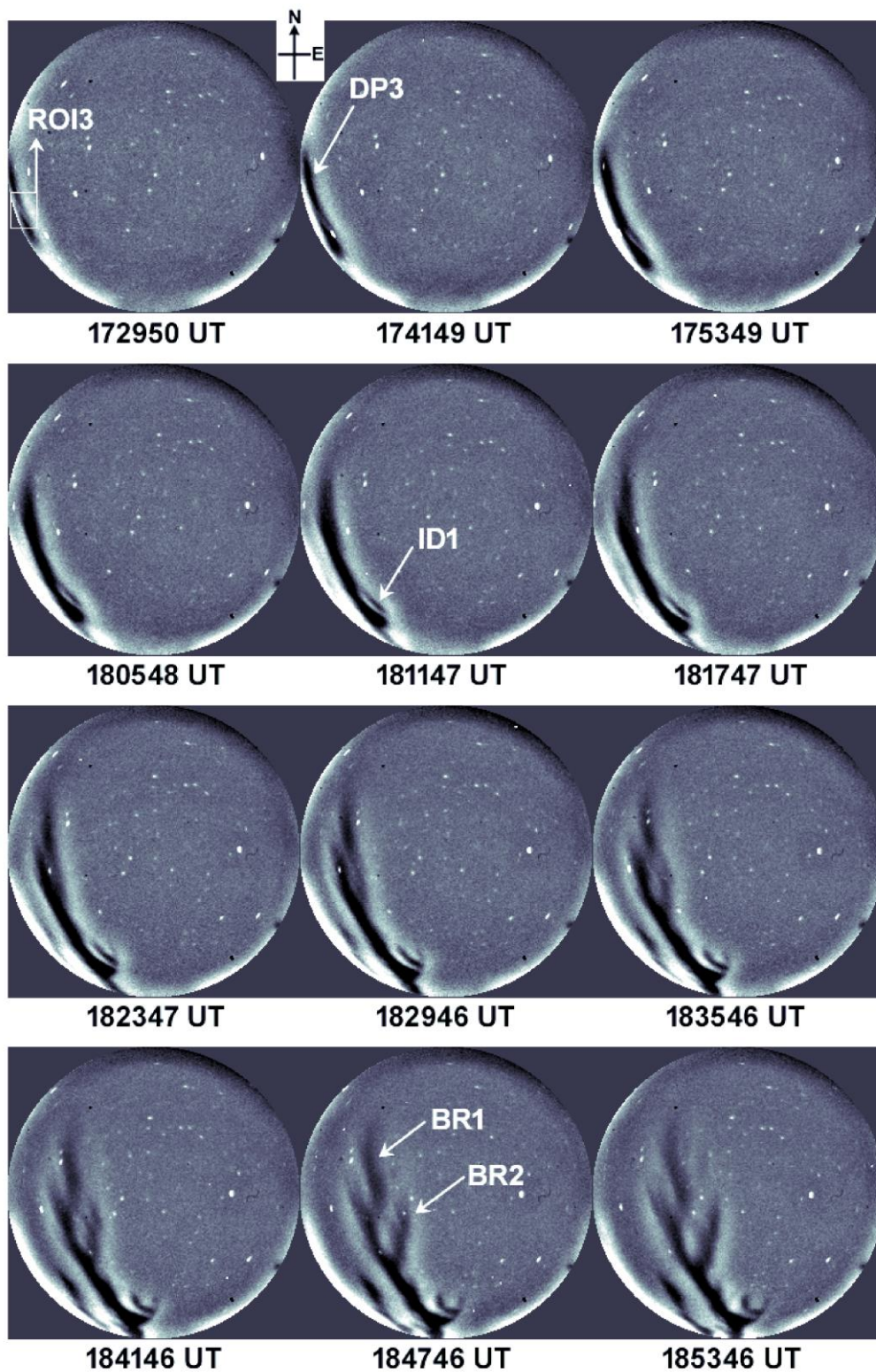
799



800

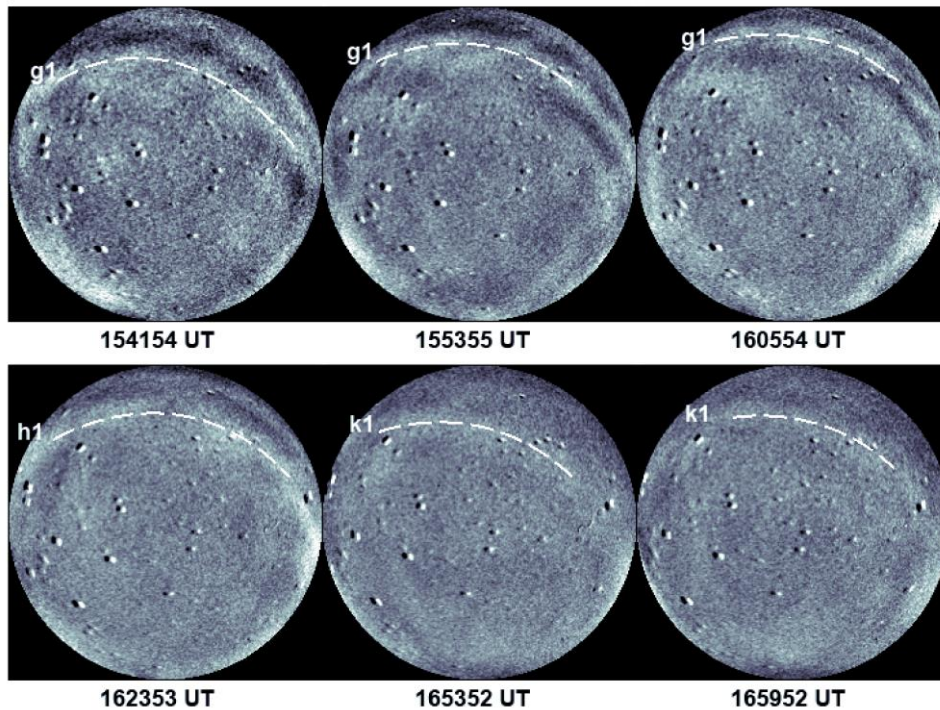
801 **Figure 5.** (a) Scatter plot of the TEC along the track of IPPs for a few GPS and GLONASS
 802 satellites (prefixed as ‘G’ and ‘R’, respectively) in the geographic grid of 5-35° N x 65-95° E
 803 during 1630-1930 UT on 16 April 2012. PRN numbers of GPS/GLONASS satellites along
 804 with the start time at 1700 UT are marked adjacent to the corresponding IPPs trajectory.
 805 G28’s trajectory lay close to the south-west sector of the ASAI. Imager’s field-of-view is
 806 shown by dashed quarter circle with its centre at Ranchi. (b) TEC variations of a few

807 GPS/GLONASS satellites showing the presence of GWs activity. (c) Mean TEC and ROTI
808 variation over Hyderabad (17.3° N, 78.6° E, mlat. ~12.0° N, located equatorward of Ranchi).
809



810
811 **Figure 6.** Selected ASAI images showing the revival of fossil depletion **DP3** during 1730-
812 1854 UT on 06 March 2013 over Ranchi. **ROI3** is the region-of-interest wherein depletion

813 **DP3** appeared sliced by an unclear thin streak of slightly enhanced airglow. **BR1** and **BR2**
814 are two structuring that developed on its east wall.
815



816
817 **Figure 7.** Limited time difference ASAI images showing GW activity during 1530-1700 UT
818 on 06 March 2013. Beginning 1336 UT, GW signatures were seen in airglow images;
819 however, activity intensified during 1530-1736 UT. Some of clear GW fronts are marked as
820 'g1', 'h1' and 'k1'.

821 **Supplementary Material**

822 **Supplementary Material S1:** Movie created from all-sky 630 nm nightglow images
823 showing the gravity wave activity and the evolution of depletion DP1 and DP2 (available
824 from <https://doi.org/10.5281/zenodo.10829073>).